TITLE: STATISTICAL ESTIMATION OF THE POSITION OF AN APEX: APPLICATION TO THE GEOLOGICAL RECORD

RUNNING TITLE: STATISTICAL ESTIMATION OF AN APEX

AMANDA OWEN[1*], PETER E. JUPP[2], GARY J. NICHOLS[1**], ADRIAN J. HARTLEY[3], GARY S. WEISSMANN[4], DINARA SADYKOVA[5]

[1]Department of Earth Sciences, Royal Holloway, University of London, Egham, TW20 0EX.

[2] School of Mathematics and Statistics, University of St. Andrews, St. Andrews, Fife, KY16 9SS, U.K.

[3] Department of Geology and Petroleum Geology, School of Geosciences, University of Aberdeen, Aberdeen, AB24 3UE, U.K.

[4] Department of Earth and Planetary Sciences, MSC03 2040, 1 University of New Mexico, Albuquerque, New Mexico 87131-0001, U.S.A.

[5] Centre for Research into Ecological and Environmental Modelling, University of St. Andrews, St. Andrews, Fife, KY16 9LZ, U.K.

*Now at: Department of Geology and Petroleum Geology, School of Geosciences, University of Aberdeen, Aberdeen, AB24 3UE, U.K.

**Now at: Nautilus Limited, Ashfields Farm, Priors Court Road, Hermitage, Berkshire, RG18 9XY, U.K.

Email: a.owen@abdn.ac.uk

Keywords: Distributive systems; point-source; apex; confidence region; maximum likelihood.

## ABSTRACT

Knowing the position of an apex of a distributive depositional system can provide important spatial constraints on paleogeographic reconstructions, and thus can greatly help facies predictions, at both a system and a basin scale. To date, predicting the position of an apex of a sedimentary system is often limited to generalized statements based on facies mapping and qualitative analyses of paleocurrent readings. This paper presents a user-friendly quantitative methodology based on the von Mises distribution and uses the method of maximum likelihood to obtain an estimated apex and associated confidence regions for a dataset. The methodology presented has been applied to two modern distributive fluvial systems (DFSs), the Taquari DFS, situated in southwestern Brazil, and the Gilbert DFS, situated in northwestern Queensland, Australia. The position of each apex is known for the two systems, thus allowing the accuracy of the methodology to be tested. A range of datasets, within which the amount and spatial distribution of localities were selected independently, was analyzed. The predicted apices came within encouraging proximity of the true apices, ranging in distance from 2.7 km to 40.3 km (1.6 to 23.4% of the total DFS length) away, with accuracy generally increasing with increasing dataset size and proximity to the apex. Data collected from the Late Jurassic Salt Wash DFS were also analyzed using the code. Results have helped to give better geographical constraints on the system and apex location as well as on the southern margin of the Morrison depositional basin. Although tested on modern and outcrop-based datasets from DFS, the methodology can be applied to any dataset, subsurface or surface, in which dispersion occurs from a point source, thus unlocking the potential for better paleogeographic constraint on a broad range of sedimentary environments such as deltas and submarine fans.


## INTRODUCTION

Understanding the position of an apex for a point-sourced sedimentary system, such as a distributive fluvial system (DFS), delta, or submarine fan, can significantly aid paleogeographic reconstructions, as it allows an understanding of where sediment entry points into sedimentary basins are located.

This gives an understanding of sediment distribution, and therefore facies distribution, in continental, deltaic, and deep-water settings through the utilization of facies models of different depositional systems i.e., DFS, deltaic, and deep-marine-fan facies models. The distribution of reservoirs and aquifers, prior to tectonic movement, is primarily controlled at the time of deposition, and therefore understanding the location of an apex may aid exploration efforts for key commodities. At a larger scale, it allows the basin limit to be delineated better, as the apices of distributive systems are commonly found either at or close to the basin margins, i.e. the distributive pattern marks the point at which the systems aggrade, as well as aiding the identification of areas of reservoir-rich or reservoir-deficient areas i.e., megafan versus interfan areas.

To date, constraining the location of an apex has been achieved largely through mapping of facies distributions and analysis of paleocurrent datasets (e.g., Howard 1966; Hirst and Nichols 1986; Nichols 1987). However, facies-mapping efforts are often hampered by the quality and extent of outcrop exposures, or by limited borehole and seismic-reflection data coverage when analyzing subsurface systems. This has resulted in many authors being able to speculate only on the general area in which the source area of a system resides (e.g., Van de Graaff 1972; Turner-Peterson 1986). The analysis of paleocurrent data allows an understanding of flow direction to be gained, and thus provides a reference point for upstream and downstream facies predictions. When observations are taken at several localities, it may be possible to estimate the position of the apex and source area for a sedimentary system.

Jupp et al. (1987) presented a methodology that estimated the position of an apex statistically from paleocurrent readings for a distributive fluvial system (DFS) (Weissmann et al. 2010; Hartley et al. 2010). They applied this methodology to the Miocene Huesca and Luna DFSs situated in the Ebro Basin, northeastern Spain (Hirst and Nichols, 1986) and successfully estimated the apex of the Luna DFS. The results complemented estimates based on facies distributions. The approach described by

Jupp et al. (1987) is however an underutilized quantitative method for paleogeographic reconstruction, one that is now being pursued as it provides objective analyses based on quantitative directional statistics to estimate the position of an apex.

This paper aims to build upon the framework of Jupp et al. (1987) by revising and simplifying the models used. The robustness of the methodology is tested on two modern DFSs, for which the apex locations are known, and a rock-record example from the Salt Wash Member of the Upper Jurassic Morrison Formation, SW USA. The methodology uses R (R Core Team, 2014), a freely available statistical program. The information required by the end user includes paleocurrent directions and a grid reference in a simple tabular format. The code and step-by-step manual for implementation can be downloaded at http://www.mcs.st-andrews.ac.uk/~pej/apex.html. The original data used in the analyses can be found as a supplementary file.

## MATHEMATICAL PRINCIPLES

In order to estimate statistically the location of an apex for a distributive system, and subsequent precision of any estimates made, it is necessary to assume that the data are generated by a particular statistical model (see Equations 1 through 3). Such a model will include the position of the apex, an unknown vector parameter denoted by $\mathbf{c}$, as well as unknown concentration parameters $\kappa_1, \ldots \kappa_s$ and mean directions $\mu_1, \ldots, \mu_s$ in Equations 2 and 3. Standard mathematical techniques can then be used to estimate the unknown parameters and so provide an estimate and confidence regions for the apex, the details of which are given in the following section.

Field observations, i.e., paleocurrent readings, can be reduced to a set of pairs $(\mathbf{x}_i, \theta_{ij})$ for $i = 1, \ldots, s$ and $j = 1, \ldots, n_i$. Here $s$ is the number of sites, $n_i$ is the number of directions observed at the $i$th site, $\mathbf{x}_i$ denotes the position vector (in the Cartesian plane) of the $i$th site, and $\theta_{ij}$ is the direction (in the interval (0, 360°)) representing the $j$th direction at the $i$th site. Reasonable statistical models for the directions $\theta_{ij}$ can be based on the von Mises distribution (Section 3.5.4 of

Mardia and Jupp, 2000; Section 3.3.6 of Fisher, 1993; Section IV(ii) of Gaile and Burt, 1980; and under the name "circular normal distribution" in Section 2.2.4 of Jammalamadaka and SenGupta, 2001; and Section 10.3 of Blaesild and Granfeldt, 2003). We assume that (i) the directions (angles) $\theta_{ij}$ $(i = 1, \dots, s, j = 1, \dots, n_i)$ are independent observations, (ii) at each site $\mathbf{x}_i$, the angles $\theta_{i1}, \dots, \theta_{in_i}$ are observations on a von Mises distribution $M(\mu_i, \kappa_i)$ with probability density function (p.d.f.) of

$$f(\theta; \mu_i, \kappa_i) = \{2\pi I_0(\kappa_i)\}^{-1} \exp\{\kappa_i \cos(\theta - \mu_i)\}, \quad 0 \leq \theta \leq 360°, \tag{1}$$

where $\mu_i$ (with $0 \leq \mu_i \leq 360°$) represents the mean direction at the $i$th site, $\kappa_i$ (with $0 \leq \kappa_i$) is a measure of concentration about $\mu_i$, and $I_0(\cdot)$ is the modified Bessel function of the first kind and order zero. A plausible statistical model, which we denote by $M_{s+2}$, for the $\theta_{ij}$ $(i = 1, \dots, s, j = 1, \dots, n_i)$ takes the p.d.f $\theta_{ij}$ to have the form Equation 1, where $\mu_i(\mathbf{c})$ is the direction from $\mathbf{c}$ to $\boldsymbol{x}_i$ and $\kappa_1, \dots, \kappa_s$ can take any non-negative values. The concentration of the distribution around $\mu_i$ increases as $\kappa_i$increases: for $\kappa_i$ near 0, the distribution of $\theta$ is almost uniform; for $\kappa_i$ large, $\theta$ is approximately normally distributed with mean $\mu_i$ and standard deviation ${\kappa_i}^{-1/2}$. In a simpler model, $M_3$, the mean directions are $\mu_1(\mathbf{c}), \dots, \mu_s(\mathbf{c})$ and $\kappa_1 = \dots = \kappa_s = \kappa$. For example, one might expect concentrations (as measures of inverse within-site paleocurrent variability) to be more variable in the distal domain than in the proximal domain of a DFS. In this respect model $M_{s+2}$, permits concentrations to vary across a DFS, while model $M_3$ assumes equal concentrations for simplicity. To assess how well model $M_{s+2}$ fits the data, model $M_{2s}$ is needed, in which $\mu_1, \dots, \mu_s$ and $\kappa_1, \dots, \kappa_s$ can take any appropriate values. Model $M_{2s}$ does not assume a different apex for each observation station, it merely allows $\mu_1, \dots, \mu_s$ not to point directly towards the single apex. These models are listed in Table 1, in which the subscript $p$ on model $M_p$denotes the number of parameters involved.

In any of the models, inference on the unknown parameters is carried out using the likelihood function. Given the observed directions $\boldsymbol{\theta} = \{\theta_{ij}\}$ for $i = 1, \dots, s$ and $j = 1, \dots, n_i$, the likelihood function $L(\mu_1, \dots, \mu_s, \kappa_1, \dots, \kappa_s; \boldsymbol{\theta})$ is defined by

$$L(\mu_i, \dots, \mu_s, \kappa_1, \dots, \kappa_s; \boldsymbol{\theta}) = \prod_{i=1}^{s} \prod_{j=1}^{n_i} f\left(\theta_{ij}; \mu_i, \kappa_i\right), \tag{2}$$

where $f\left(\theta_{ij}; \mu_i, \kappa_i\right)$ is defined by Equation 1. For the models in Table 1 the likelihood function is obtained from (2) by expressing $\mu_1, \dots, \mu_s, \kappa_1, \dots, \kappa_s$ in terms of the appropriate parameters.

For example, for $M_{s+2}$,

$$L(\boldsymbol{c}, \kappa_1, \dots, \kappa_s; \boldsymbol{\theta}) = \prod_{i=1}^{s} \prod_{j=1}^{n_i} f\left(\theta_{ij}; \mu_i(\boldsymbol{c}), \kappa_i\right). \tag{3}$$

In any of the models, a suitable method (with particularly desirable mathematical properties) for estimating the unknown parameters is maximum likelihood (e.g., Section 11.1 of Blaesild and Granfeldt, 2003; Section 7.7 of Lindgren, 1993; Section 3.2.2 of Lindsey, 1996), i.e., the estimates of the parameters are the values that maximize $L$. Thus, for $M_{2s}$ , the estimates $\hat{\mu}_1, \dots, \hat{\mu}_s, \hat{\kappa}_1, \dots, \hat{\kappa}_s$ of $\mathbf{c}, \kappa_1, \dots, \kappa_s$ maximize Equation 3. In either model, the vector $\hat{\mathbf{c}}$ is the estimated position of the apex, **c**.

An idea of the precision of the estimate, $\hat{\mathbf{c}}$ can be obtained through confidence regions (see Section 7.5.2 of Lindsey, 1996, for a detailed explanation of confidence regions). Intuitively speaking, a confidence region is a region in which the user can be, for example, 95% confident that the true apex (**c**) lies within the region. Confidence regions (99%, 95%, and 90%) are generated by the code provided.

Approximate confidence regions for **c** in models $M_{s+2}$ and $M_3$ can be obtained from the likelihood. If $n_1, \ldots, n_s$ are large, then the regions

$$\{\mathbf{c} : 2[\log L(\hat{\mathbf{c}}, \hat{\kappa}; \boldsymbol{\theta}) - \log L(\mathbf{c}, \hat{\kappa}; \boldsymbol{\theta})] \leq \chi^2_{2;\alpha}\}$$

for $M_3$ and

$$\{\mathbf{c} : 2[\log L(\hat{\mathbf{c}}, \hat{\kappa}_1, \ldots, \hat{\kappa}_s; \boldsymbol{\theta}) - \log L(\mathbf{c}, \hat{\kappa}_1, \ldots, \hat{\kappa}_s; \boldsymbol{\theta})] \leq \chi^2_{2;\alpha}\}$$

for $M_{s+2}$, are approximate $100(1-\alpha)$% confidence regions for **c**. Here $\chi^2_{2;\alpha}$ denotes the upper $100\alpha$% quantile of the $\chi^2_2$ distribution (e.g., $\chi^2_{2;0.05} = 5.99$). Various standard optimization routines are available and can be used to obtain the maximum likelihood estimates and the confidence regions for **c**. We find it convenient to use the code that we have written for this in the R language (R Core Team, 2014) for statistical computation.

Once the parameters have been estimated, the questions arise: (i) whether $M_3$ fits the data nearly as well as $M_{s+2}$, (ii) whether $M_{s+2}$ fits the data well. These can be answered using the likelihood. For $p = 3, s+1, 2s$, let $\hat{L}_p$ denote the maximum value of the likelihood for model $M_p$. Since $M_3$ can be obtained by restricting the values of some parameters of $M_{s+1}$ and $M_{s+1}$can be obtained by restricting the values of some parameters of $M_{2s}$, we have $\hat{L}_3 \leq \hat{L}_{s+2} \leq \hat{L}_{2s}$. The questions are whether $\hat{L}_{s+2}$ is significantly bigger than $\hat{L}_3$ and whether $\hat{L}_{2s}$is significantly bigger than $\hat{L}_{s+2}$. Define

$$D_{\text{same}} = 2\log(\tfrac{\hat{L}_{s+2}}{\hat{L}_3}) \quad \text{and} \quad D_{\text{fit}} = 2\log\left(\tfrac{\hat{L}_{2s}}{\hat{L}_{s+2}}\right).$$

The deviances $D_{same}$ and $D_{fit}$ measure the differences between $M_3$ and $M_{s+2}$, and between $M_{s+2}$ and $M_{2s}$, respectively. The method of likelihood ratio tests allows a choice to be made between nested models (e.g., Section 12.5 of Gilchrist, 1984) and leads to the following tests. If $D_{same}$ is large compared with the $\chi^2_{s-1}$ distribution, or equivalently the $P$-value (the probability of getting a value of $D_{same}$ at least as large as that observed) for testing $M_3$ against $M_{s+2}$ is small, then we conclude that $M_{s+2}$ gives a significantly better fit to the data than $M_3$ does, i.e., it is worth the extra

complexity of $M_{s+2}$ in order to obtain a better fit. If the *P*-value given by $D_{same}$ is large, then we conclude that it is worth sacrificing the better fit of $M_{s+2}$ in order to describe the data more concisely by $M_3$ . Similarly, if $D_{fit}$ is large compared with the $\chi^2_{s-2}$ distribution, or equivalently if the $P$-value for testing $M_{s+1}$ against $M_{2s}$ is small, then we conclude that it is worth the extra complexity of $M_{2s}$ to get a better fit. If the *P*-value given by $D_{fit}$ is large, then we conclude that it is worth sacrificing the better fit of $M_{2s}$ in order to describe the data more simply by $M_{s+2}$.

In certain contexts, some of the observations are axial, e.g., a channel-edge reading, where it is not possible to distinguish between the angles $\theta$ and$\theta + 180°$. In this case, one can use variants of the models above, as indicated in Jupp et al. (1987).

## APPLICATION TO MODERN DFSs

Both the Gilbert DFS, situated in northwestern Queensland, Australia, and the Taquari DFS, situated in southwestern Brazil, (Fig. 1) are covered by good satellite imagery in which the apex and channels, both active channels and paleochannels, are visible across the DFS surface. Both DFSs appear to have experienced a minor degree of human modification and thus provide suitable candidates for testing the methodology.

Grids, composed of 10 km by 10 km cells, were placed onto each DFS. Where satellite imagery allowed, 10 directional measurements were obtained along channel, or paleochannel reaches, within each cell (Fig 2). The measurements within each cell were assigned to one central grid reference to help simulate variability of flow directions typically experienced in a vertical succession at geological outcrops. A 10 km by 10 km cell size was chosen, as it was deemed large enough to capture channel sinuosity, and therefore directional variability, within channel reaches. For each DFS, the directions at 30, 20, 15, and 10 independently selected locations were selected using the "random" function in Excel and then analyzed using the methodology. An analysis of the full database for each DFS was also run for comparison purposes. Further analyses were conducted in

which the positions of 20 independently selected sites were restricted to proximal, medial, or distal portions of the DFS to see how important the spatial distribution of data is when trying to estimate the position of an apex.

*Taquari DFS*

The Taquari DFS has an apex-to-toe length of approximately 250 km and an area of approximately 50,000 km$^2$ (Assine 2005). The Taquari DFS is situated in the Pantanal Basin, which has been characterized as being a backbulge depozone by Horton and DeCelles (1997) or a small extensional basin of the eastward-migrating forebulge of the Andes system by Ussami et al. (1999). It is currently depositing sediment under a tropical subhumid climate, with warm (32°C) and wet conditions persisting during summer months, and slightly cooler (21°C) and drier conditions prevailing in winter months (Assine 2005).

**Results.---**

All the datasets obtained from the Taquari DFS, with the exception of the Taquari proximal dataset, have P-values of < 0.05 in the "*p.fit*" column of Table 2. The small P-values indicate that, in each case, model $M_{2s}$ fits the dataset significantly better than model $M_{s+2}$. Thus, statistically, none of these datasets supports the notion that almost all of the mean directions point directly away from a single apex i.e., there is local variability in paleocurrent directions that deviate away from a perfect fan morphology. This is to be expected in natural systems and is illustrated in Figure 3 in several plots. However, taking a broad view of the datasets it is clear that, generally, the mean directions suggest the presence of a single apex. To obtain this conclusion statistically would require the use of more sophisticated models than we have considered here; the few simple models considered here have been chosen for their general applicability to a host of systems. Based on the assumption that a single apex is present, the small P-values (< 0.05) in the "*p.same*" column of Table 2 suggest that model $M_{s+2}$ fits the data significantly better than model $M_3$ does for Taquari full, 30, 15, and 10

datasets. The Taquari 20, medial and distal datasets, however, are different in that a P-value of > 0.05 is observed, suggesting that model $M_3$ fits the data almost as well as model $M_{s+2}$, indicating that the locations have approximately equal concentrations, and thus model $M_3$ can be used.

For the Taquari proximal dataset, the value of *p.fit* is > 0.05 (Table 2), indicating that model $M_{s+2}$ fits this dataset almost as well as model $M_{2s}$, supporting statistically the notion that the mean directions point almost directly away from a single apex. Once model $M_{s+2}$ has been selected, the question arises of whether or not model $M_3$ would fit the data almost as well as model $M_{s+2}$ i.e., whether or not the locations have approximately equal concentrations. The value of *p.same* is < 0.05, demonstrating that model $M_{s+2}$ fits the dataset significantly better than model $M_3$, indicating the locations have significantly different concentrations, so that model $M_{s+2}$ fits the data better.

In order to determine how close the estimated apices were to the true apex, the estimated apex from the best-fitting model from each dataset was plotted onto the Taquari DFS. For clarity, the estimated apices for models that did not fit the data best were not plotted. However, as can be seen in Table 2, they are often situated close to the estimated apex given by the best-fitting model. As can be seen in Table 2 and Figures 3 and 4, and as would be expected, the Taquari full dataset estimated the apex closest to the true apex, placing it 13.1 km away, closely followed by datasets Taquari proximal (15.4 km away) and Taquari 30 (19.7 km away), all of which have confidence regions that contain or are very close to the true apex. The analysis of dataset Taquari 10 estimates the apex the farthest away, placing it outside of a realistic region, followed by Taquari medial (42.4 km away), Taquari distal (40.3 km away), Taquari 15 (34.2 km away), and Taquari 20 (30.6 km away), with confidence regions again containing or being close to the true apex. The confidence regions are larger for the datasets in which the estimated apices are farther from the true apex. Although none of the datasets produces an estimated apex which is exactly equal to the true apex, the estimated apices from the Taquari full, Taquari 30, Taquari proximal, and Taquari distal datasets come within a

credible distance of the true apex i.e., ranging from as close as 5.2% of the total DFS length away from the true apex to < 10%, with all other datasets lying within 17% of total DFS length.

As can be seen in Figures 3 and 4A, nearly all datasets place the apex north of the true apex. Presumably this is a consequence of recent incision on the DFS where the incised portion has a sharp bend northwards of the old apex (Fig. 4). The channels that radiate outwards from the currently more active lobe of the DFS is therefore causing a skew in results, whereby the estimated apex is farther north than the true apex. This bend is evident in satellite imagery (Fig 4), and was not sampled in any of the datasets, with the exception of the Taquari full dataset. In the case of the Taquari full dataset, although the sharp bend is visible in Figure 3A and 4A, the methodology gives observations at sites near the bend the same weighting as all other sites, and thus these observations are eclipsed by the other readings. Despite placing the apex north of the true apex, the estimated apices from datasets Taquari full and Taquari 15 place the apex very close the basin margin edge (1.3 km and 14.5 km away), with all other datasets, with the exception of Taquari 10, placing the apex <34.8 km away (an error <14% of total DFS length).

When analysing estimates for the Taquari 10 dataset, an unrealistic estimate is provided by the code. This is considered to be the result of nearly four of the ten arrows (located in the southwestern portion of Fig. 3E) being nearly parallel to one another. As the directions of nearly half the dataset point in a southward direction, the estimate of the apex is pushed to the northeast. Because the directions are almost parallel, they give little information about how far away the apex is. This results in uncertainty and an unrealistic position of the apex in a northeast-southwest transect. Interestingly, unrealistic estimates are also given for model $M_3$ for Taquari 30 and 15 datasets (Table 2). We speculate that, due to model $M_{s+2}$ giving credible results, the concentrations, which is what differentiates model $M_3$ from model $M_{s+2}$, are very different, thus the simpler $M_3$ model provides an improbable result.

*Gilbert DFS*

The Gilbert DFS is smaller than the Taquari DFS, possessing an apex-to-toe length of approximately 170 km and an area of approximately 12,500 km$^2$. The Gilbert DFS is currently depositing under a tropical savannah climate in which monsoonal climate conditions prevail in an intracratonic basin that has been slowly subsiding since the Late Tertiary (Jones et al. 1993). This tectonic framework coupled with continued sediment supply has resulted in the progradation of the Gilbert DFS into the relatively shallow Gulf of Carpentaria (Nanson et al. 2013), where the toe of the DFS is currently being reworked by marine processes.

**Results.---**

The P-values shown in Table 3 indicate for all of the datasets that model $M_{2s}$ fits the data significantly better than model $M_{s+2}$ , implying that assuming that the mean directions point away from a single apex is too simple an approach to the data, due to local variability in mean directions. However, when it is assumed that the mean directions point away from a single apex, a safe assumption to make when taking a generalized overview of the datasets (Fig. 5), $M_{s+2}$ gives a significantly better fit than model $M_3$ for all datasets, excluding Gilbert medial, where model $M_3$ fits the data best.

As can be seen in Table 3 and Figures 4 and 5, the Gilbert proximal dataset estimates the position of the apex most accurately, placing it only 2.7 km away from the true apex, followed by the datasets Gilbert full (9.4 km away), Gilbert 20 (9.5 km away), and Gilbert 30 (11.3 km away). The dataset Gilbert 15 places the apex farthest away, estimating it to be 39.8 km away from the true apex, followed by datasets Gilbert medial (39.2 km away), Gilbert 10 (35.8 km away), and Gilbert distal

(27.7 km away). Broadly speaking, the size of the confidence regions increases with increasing distance between the estimated apex and the true apex, except for the Gilbert medial dataset. As can be seen in Figure 5G, the randomly selected sites of the Gilbert medial dataset display a clear radial morphology, and as a result of this the estimated apex position is "pulled" closer to the medial localities and away from the true apex. As with the Taquari simulations, the estimated apices come within a distance of the true apex, with proportional margin of error ranging from 1.6% (Gilbert proximal dataset) to 23.4% of the total DFS length (Gilbert medial dataset), the majority of simulations being within 20% of the total DFS length away from the apex (Table 3).

In contrast to the majority of datasets for the Taquari DFS, for the Gilbert DFS the true apex lies within the confidence regions for all datasets except the Gilbert medial dataset (Fig 5). We consider that this is due to the more elongated morphology that the Gilbert DFS has in comparison to the Taquari DFS (Fig 4), and therefore the estimated apices broadly align on the northwest-southeast-trending axis of the DFS with little lateral variability from this line. Thus the confidence regions contain the true apex. The central axis of the DFS has therefore been estimated accurately by the methodology with the apices varying along this axis. This is opposite to the results of the Taquari DFS datasets, which have confidence regions that possess a more circular form with predicted apices that pinpoint the location of the basin margin more accurately, but to the north of the central axis of the system. We speculate that the difference is a function of the Taquari DFS possessing a more radial rather than elongated fan morphology and a consequence of the newly developed lobe and associated incision of the trunk channel.

## *Discussion*

The analyses of the modern datasets indicate that although it is commonly the case that more data will provide more accurate estimates, this is not always true. For example, dataset Gilbert 20 (Fig. 5C) provides a more accurate estimate of the apex than dataset Gilbert 30 (Fig. 5B), and Taquari proximal (Fig. 3F) provides a closer estimate than Taquari 30 (Fig. 3B). When the locations of the data are restricted, datasets that use only proximal data produce the most accurate estimates for both DFSs. However, when data are restricted to just medial or distal sections, there does not appear to be a clear trend of accuracy in estimates. For example, the estimated apex for the Gilbert distal dataset (Fig. 5H) is closer to the true apex than the predicted apex for the Gilbert medial dataset (Fig. 5G), while the estimated apex for the Taquari medial dataset (Fig. 3G) is closer to the true apex than is the estimated apex from the Taquari distal dataset (Fig. 3H). We consider the that the analyses of the proximal datasets give the most accurate estimates, because the channel orientation readings have a radial pattern over a much smaller area than in the medial and distal datasets. Therefore, by limiting the area the accuracy of the estimate of the true apex increases. The most accurate results obtained are generally from datasets that express a consistent radial pattern over a good spatial area which includes proximal localities, such as the Taquari medial and 30 datasets (Fig. 3G and B) and the Gilbert proximal and 20 datasets (Figs. 5F and C). However, all other datasets give encouraging results, in that all estimated apices, with the exception of those from the Taquari 10 dataset, are <17% of the total DFS length away from the true apex for the Taquari DFS, and within 24% of the total DFS length away from the true apex for the Gilbert DFS.

Based on the analyses of datasets from the Taquari and Gilbert DFSs, the methodology provides credible estimates of the position of an apex. Statistical models with more parameters may give even closer estimates of the apex by adding extra parameters and rules that will take local conditions into account. For example, marine reworking and its effect on paleocurrent directions at the toe of the Gilbert DFS could be incorporated into the models. Also, heavier weighting could be provided to readings that highlight the change in the main trunk channel direction from northwest

to west on the Taquari DFS. However, being able to make such observations within the geological record is rare, and it is not the aim of this paper to pinpoint the exact location of the apex for the two systems, but rather to provide a general methodology that can be applied to a host of systems that were deposited under varying local conditions.

It is important to stress that the models $M_{s+2}$ and $M_3$ assume that the mean directions point away from a single apex, and thus if the estimated apex position is to be used, it is up to the user to decide that such an assumption can be made based on geological observations and the use of *p.fit*.

## APPLICATION TO THE ROCK RECORD – THE SALT WASH DFS

To apply the methodology outlined above to an ancient dataset, we conducted an analysis on data collected from the Salt Wash fluvial system. Craig et al. (1955) and Mullens and Freeman (1957) interpreted the Salt Wash Member of the Upper Jurassic Morrison Formation as the deposits of a DFS that extended over the southwestern portion of the Colorado Plateau, USA (Fig. 6). Mapping and facies analyses conducted by Peterson (1980, 1984a), Kjemperud et al. (2008), and Weissmann et al. (2013) more recently revealed that the underlying Tidwell Member (Fig. 6), composed of minor fluvial and lacustrine facies, represents the distal facies of the prograding Salt Wash DFS. Thus the Salt Wash DFS is lithostratigraphically composed of both the Salt Wash and Tidwell Members.

The details of the tectonic configuration of the western USA during the Late Jurassic are contentious (Decelles 2004; Decelles and Burden 1991; Currie 1997; Currie 1998; Heller et al. 1986; Lawton 1994; Dickinson and Lawton 2001). These authors generally agree that a broadly northwest to southeast compressional regime existed, whereby an eastward-dipping subduction of the paleo-Pacific Farallon plate occurred below the northwestward-propagating North American plate (Decelles 2004; Turner and Peterson 2004). Compression was not uniform across the margin, in a much as the northern portion experienced an orthogonal compressional regime which resulted in a shortening of the crust and the formation of the Sevier Highlands (Decelles, 2004). The southwestern margin experienced a compressional regime that was nearly parallel to the margin, resulting in a sinistral strike-slip

intracontinental rifting phase and the formation of elevated rift shoulders, the Mogollon Highlands (Dickinson and Lawton 2001; Decelles 2004; Turner and Peterson 2004). Turner and Peterson (2004) interpreted the Mogollon Highlands, bounding the southern margin of the depositional basin, and the Sevier Highlands, bounding the western margin of the depositional basin, to be key sediment sources for the Morrison Formation.

Attempts in the past to constrain the source area and apex location for the Salt Wash DFS are of a general nature. For example, Robinson and McCabe (1997) noted, based on paleocurrent data and facies observations, that the Salt Wash fluvial system had its source in an area west and southwest of Shootering Canyon, Utah, located in Figure 6. Craig et al. (1955), based on analyses of paleocurrent data, facies and thickness patterns, postulated that the apex for the Salt Wash DFS was positioned somewhere within west-central to northwestern Arizona, southeastern California, and southern Nevada. Mullens and Freeman (1957) suggested that the apex was situated in south-central Utah, based on the thickest portion of the Salt Wash being preserved there. However, the interpretation given by Mullens and Freeman assumes that the deposits are the most proximal deposits of the original system, rather than being the most proximal deposits preserved and exposed.

Other authors, such as Peterson (1984b) and Dickinson and Gehrels (2008) attempted to identify a source area rather than apex location for the Salt Wash DFS. Based on petrology and mapping studies, Peterson (1984b) stated that most of the sediment found in the Salt Wash and Tidwell Members was derived from a source area situated more than 160 km southwest and 100 km west of outcrops in northeastern Arizona, with only some of the material for the system coming from older Mesozoic formations in the southwestern and western parts of the region. Dickinson and Gehrels (2008) postulated from U-Pb detrital-zircon data that it is feasible that the Salt Wash DFS could have, either wholly or partly, been sourced from the Mogollon highlands, located in Figure 7. It is clear

from a review of the literature that there is a high range of uncertainty about pinpointing the apex of the Salt Wash fluvial system, with current estimates spanning an area of approximately 50,000 km$^2$.

In an attempt to constrain the location of the Salt Wash DFS apex better, we applied 749 paleocurrent readings from 27 localities across the system (Fig. 6) using the methodology outlined above. At each locality, paleocurrent readings from sedimentary structures (trough and planar cross-bedding) in different sandstone bodies were combined and assigned to one grid- reference, to maintain a system-scale overview of paleoflow direction. All paleocurrent readings were, when applicable, corrected for later structural dip. It is noted that the measurements taken from bedforms from the Salt Wash DFS are not directly analogous to the channel orientations taken from the two presented modern datasets. As noted by Miall (1974), directional variance increases with decreasing structure scale. However, identifying comparable structure scales for the ancient and modern datasets is not possible, due to the difficulties with taking cross-bedding measurements from modern systems, and alternatively channel orientations from the ancient. We envisage that by taking several measurements along channel reaches within individual 10 km by 10 km cells, and centralizing all readings to a point in the center of the cell, the variability observed within smaller structures in the rock record is imitated.

*Results and Geological Implications*

As can be seen in Table 4, model $M_{2s}$ fits the data better than model $M_{s+2}$. Based on the analyses of facies distributions and paleocurrent readings spatially across the system, we consider it geologically sound to assume that the Salt Wash DFS had a single apex. P-values generated by the code indicate that under the assumption that the mean directions point away from a single apex, model $M_{s+2}$ fits the data better than model $M_3$ (Table 4). The estimated apex position and associated confidence regions for model $M_{s+2}$ are shown in Figure 7.

The estimated apex for model $M_{s+2}$ is located in northwestern Arizona, 160 km northwest of Flagstaff, Arizona; 250 km northeast of Las Vegas, Nevada, and 125 km southeast of Saint George, Utah (Fig. 7), which is within the predicted area given by Craig et al. (1955). The results are consistent with the geological assumptions that the Salt Wash DFS had a single apex and imply that the Salt Wash DFS had an apex-to-toe length of approximately 550 km and that approximately 150 km of proximal material is either unexposed or removed by postdepositional erosion. The results complement observations made in the field, where it was noted the most proximal deposits exposed on the system do not represent true proximal deposits in that they possess a relatively low net to gross (74% sand), which is considered to be relatively low based on descriptions given by Nichols and Fisher (2007) and Weissmann et al. (2013) for proximal DFS deposits.

Paleogeographic maps published by Decelles nd Currie (1996) and Decelles (2004) show the thrust front to be located in western Utah close to the Nevada border during the Late Jurassic, which is much farther west than the estimated apex. We therefore postulate that the Salt Wash DFS was sourced from the Mogollon-Sevier highlands syntaxis or from the Mogollon Highlands proper to the south. This is in line with statements made by Dickinson and Gehrels (2008). The results suggest that the Mogollon highlands were farther north than suggested in the paleogeographic maps of Currie (1997) and Turner and Peterson (2004), but agree with the extent mapped by Spencer et al. (2011). The results also suggest that the western margin of the basin indicated by Turner and Peterson (2004) is too far to the east. The paleogeography of the basin, and in turn the tectonics of the basin, could be further constrained with the application of the methodology presented in this paper to other fluvial systems found in the basin.

At a smaller scale, understanding the location of the Salt Wash DFS apex provides scope to build a robust facies model for the system, because sites can be more accurately placed on the system, thus enabling a more quantitative understanding (i.e., distance downstream) of facies variability on the system.

## WIDER IMPLICATIONS AND CONCLUSIONS

We have tested the methodology presented here and applied it to data obtained from satellite imagery and an outcrop DFS. Clearly, however, it can be applied more widely to any geological system that has a dispersive pattern from a point source. This methodology therefore has great potential in helping to constrain better a host of sedimentary systems, such as deltaic, submarine-fan, and alluvial-fan environments. Through this, a greater understanding of the paleogeography of an area can be gained. For example, by estimating the point source of a trough mouth fan, a fan that forms at the ice-margin front (Vorren and Laberg 1997), it may be possible to constrain paleo-ice-sheet extent better. Likewise, through the analyses of paleocurrents collected from deltaic systems, the extent of ancient shorelines can potentially be gauged. We anticipate that this methodology will be best suited to systems that crop out over large areas such as the Cretaceous systems spanning across Utah. Subset analyses are also possible with large datasets, allowing the identification of different lobes or progradation events, or even the identification of separate systems in stratigraphic units that have been mapped as basin fills, i.e., accurately mapping the Recapture and Westwater Canyon systems in the Morrison Basin (Craig et al. 1955). The methodology can be used at a variety of scales, which is important to identify when applying the methodology; if data from a single lobe are used, the methodology will predict the apex of that particular lobe, if data across a system are used, it will find the apex of a system. The application of the methodology is not restricted to sedimentary systems, as is demonstrated by Jupp and Spurr (1989), who estimate the three-dimensional position of a shock center for a volcanic shatter cone situated on the Slate Islands, Lake Superior, Canada.

Because directional indicators, such as channel orientations in three-dimensional seismic or bedform readings from borehole formation micro-imaging (FMI) data, can now be more readily gained, the methodology presented here is readily applicable also to subsurface datasets, when data are

available either at or near the system scale, or data points are located in the proximal or medial portions of the systems, as is demonstrated in the worked examples from the Gilbert and Taquari DFS datasets.

In conclusion, a methodology that estimates the position of an apex statistically is presented and is tested on two modern DFS datasets, for which the location of the apex is known. Although confidence regions may be large when data are limited or highly variable, the methodology described provides an improved objective predictive tool for the geologist to constrain better the extent of depositional systems, enabling data points to be put into a system-scale context. Data from the Late Jurassic Salt Wash DFS are also analyzed, with results complementing field observations and shedding light onto the paleogeography of both the sedimentary basin and the Salt Wash DFS. Due to the user-friendly nature of the methodology presented and provided, this methodology is an attractive predictive tool for use on data obtained from outcrop-based and potentially subsurface-based studies.

## ACKNOWLEDGMENTS

The authors would like to thank BG, Chevron, ConocoPhilips, and Total for sponsoring Phase 1 of the Fluvial Systems Research Group consortium which funded the PhD project researching the Salt Wash DFS. Initial discussions with David Waltham are greatly appreciated. We also appreciate constructive comments from reviewers Chris Paola and Mike Blum, and Associate Editor Paul McCarthy which improved the manuscript. The authors would also like to thank Anna Kulikova, Guy Prince, Kelsey McNamara and Karen Oud for assistance in the field.

## REFERENCES

Assine, M.L., 2005, River avulsions on the Taquari megafan, Pantanal wetland, Brazil: Geomorphology, v. 70, p. 357–371.

Blaesild, P., and Granfeldt, J., 2003, Statistics with Applications in Biology and Geology: Boca Raton, Chapman and Hall/CRC, 568 p.

Craig, L.C., Holmes, C.N., Cadigan, R.A., Freeman, V.L., Mullens, T.E., and Weir, G.W., 1955. Stratigraphy of the Morrison and related formations Colorado Plateau Region, a preliminary report: US Geological Survey, Bulletin 1009-E, p. 125–168.

Currie, B.S., 1997, Sequence stratigraphy of nonmarine Jurassic – Cretaceous rocks , central Cordilleran foreland-basin system: Geological Society of America, Bulletin, v. 109, p. 1206–1222.

Currie, B.S., 1998, Upper Jurassic-Lower Cretaceous Morrison and Cedar Mountain Formations, northeastern Utah-northwestern Colorado: Relationships between nonmarine deposition and Early Cordilleran foreland-basin development: Journal of Sedimentary Research, v. 68, p. 632–652.

Decelles, P.G., 2004. Late Jurassic to Eocene evolution of the Cordilleran thrust belt and foreland basin system, western U.S.A.: American Journal of Science, v. 304, p. 105–168.

Decelles, P.G., and Burden, E.T., 1991, Non-marine sedimentation in the overfilled part of the Jurassic-Cretaceous Cordilleran foreland basin: Morrison and Cloverly Formations, central Wyoming, USA: Basin Research, v. 4, p. 291–313.

Decelles, P.G., and Currie, B.S., 1996, Long-term sediment accumulation in the Middle Jurassic – early Eocene Cordilleran retroarc foreland-basin system: Geology, v. 24, p. 591–594.

Dickinson, W.R., and Gehrels, G.E., 2008, Sediment delivery to the Cordilleran foreland basin: Insights from U-Pb ages of detrital zircons in Upper Jurassic and Cretaceous strata of the Colorado Plateau: American Journal of Science, v. 308, p. 1041–1082.

Dickinson, W.R., and Lawton, T.F., 2001, Tectonic setting and sandstone petrofacies of the Bisbee basin (USA–Mexico): Journal of South American Earth Sciences, v. 14, p. 475–504.

Fisher, N.I., 1993. Statistical Analyses of Circular Data, Cambridge: Cambridge University Press, 277 p.

Gaile, G.L., and Burt, J.E., 1980, Directional statistics: Concepts and techniques in modern Geography: Geo Abstracts, 25, Norwich: University of East Anglia

Gilchrist, W., 1984, Statistical Modelling: Chichester, UK, Wiley, 356 p

Hartley, A.J., Weissmann, G.S., Nichols, G.J., and Warwick, G.L., 2010, Large distributive fluvial systems: Characteristics, distribution, and controls on development: Journal of Sedimentary Research, v. 80 [2], p. 167–183.

Heller, P.L., Bowdler, S.S., Chambers, H.P., Coogan, J.C., Hagen, E.S., Shuster, M.W., and Winslow, N.S., 1986, Time of initial thrusting in the Sevier orogenic belt , Idaho-Wyoming and Utah: Geology, v. 14, p. 388–391.

Hirst, J.P.P., and Nichols, G.J., 1986. Thrust tectonic controls on Miocene alluvial distribution patterns, southern Pyrenees, *in* Allen, P.A., and Homewood, P., eds, Foreland Basins: International Association of Sedimentologists, Special Publication 8, p. 247-258.

Horton, B.K., and DeCelles, P.G., 1997, The modern foreland basin system adjacent to the Central Andes: Geology, v. 25, p. 895-898.

Howard, J.D., 1966. Patterns of sediment dispersal in the Fountain Formation of Colorado: Mountain Geologist, v. 3, p. 147–153.

Jammalamadaka, S.R., and SenGupta, A., 2001, Topics in Circular Statistics: London, World Scientific, 336 p.

Jones, B.G., Martin, G.R., and Senapati, N., 1993, Riverine-tidal interactions in the monsoonal Gilbert River fandelta, northern Australia: Sedimentary Geology, v. 83, p. 319–337.

Jupp, P.E., Spurr, B.D., Nichols, G.J., and Hirst, J.P.P., 1987. Statistical estimation of the apex of a sediment distribution system from paleocurrent data: Mathematical Geology, v. 19, p. 319–333.

Jupp, P.E., and Spurr, B.D., 1989, Statistical estimation of a shock center: Slate Islands astrobleme: Mathematical Geology, v. 21, p. 191–198.

Kjemperud, A.V., Schomacker, E.R., and Cross, T.A., 2008, Architecture and stratigraphy of alluvial deposits, Morrison Formation (Upper Jurassic), Utah: American Association of Petroleum Geologists, Bulletin, v. 92, p. 1055–1076.

Lawton, T.F., 1994, Tectonic setting of Mesozoic sedimentary basins, Rocky Mountin region, United States, *in* Caputo, M.V., Peterson, J.A., and Franczyk, K.J., eds, Mesozoic Systems of the Rocky Mountain Region USA.:SEPM, Rocky Mountain section, p. 1–25.

Lindgren, B. W., 1993, Statistical Theory, Fourth Edition: Florida, U.S.A., Chapman & Hall/CRC, 648 p.

Lindsey, J.K., 1996, Parametric Statistical Inference: Oxford, U.K., Oxford University Press, 512 p.

Mardia, K. V., and Jupp, P.E., 2000, Directional Statistics: New York, Wiley, 456 p.

Miall, A.D., 1974, Paleocurrent analysis of alluvial sediments: A discussion of directional variance and vector magnitude: Journal of Sedimentary Petrology, v. 44, p. 1174-1185.

Mullens, T.E., and Freeman, V. L., 1957, Lithofacies of the Salt Wash Member of the Morrison Formation, Colorado Plateau: Geological Society of America, Bulletin, v. 68, p. 505–526.

Nanson, R.A., Vakarelov, B.K., Ainsworth, R.B., Williamsm F.M., and Price, D.M., 2013, Evolution of a Holocene, mixed-process, forced regressive shoreline: The Mitchell River delta, Queensland, Australia: Marine Geology, v. 339, p. 22–43.

Nichols, G.J., 1987, Structural controls on fluvial distributary systems- the Luna system, northern Spain, *in* Ethridge, F. G., Flores, R.M., and Harvey, M. D., eds, Recent Developments in Fluvial Sedimentology: SEPM, Special Publication 39, p. 269–277.

Nichols, G.J. and Fisher, J.A., 2007, Processes, facies and architecture of fluvial distributary system deposits: Sedimentary Geology, v. 195, p. 75–90.

Peterson, F., 1980, Sedimentology of the Uranium-bearing Salt Wash Member and Tidwell unit of the Morrison Formation in the Henry and Kaiparowits Basin, Utah: Utah Geological Association, Publication 8, Henry Mountain Symposium, p. 305–322.

Peterson, F., 1984a, Fluvial sedimentology on a quivering craton: Influence of slight crustal movements on fluvial processes, Upper Jurassic Morrison Formation, Western Colorado Plateau: Sedimentary Geology, v. 38, p. 21–49.

Peterson, F., 1984b, Jurassic Paleotectonics in the west-central part of the Colorado Plateau, Utah and Arizona, *in* Peterson, J.A., ed, Paleotectonics and Sedimentation, Rocky Mountain Region, United States: American Association of Petroleum Geologists, Memoir 41, p. 563–596.

R Core Team, 2014, R: A language and environment for statistical computing *In* R Foundation for statistical computing, available at: http://www.r-project.org/.

Robinson, J.W., and McCabe, P.J., 1997, Sandstone-body and shale-body dimensions in a braided fluvial system: Salt Wash Sandstone Member (Morrison Formation), Garfield County , Utah: American Association of Petroleum Geologists, Bulletin, v. 8, p.1267–1291.

Spencer, J.E., Richard, S.M., Gehrels, G.E., Gleason, J.D., and Dickinson, W.R., 2011, Age and tectonic setting of the Mesozoic McCoy Mountains Formation in western Arizona, USA: Geological Society of America, Bulletin, v. 123, p. 1258–1275.

Turner, C.E, and Peterson, F., 2004, Reconstruction of the Upper Jurassic Morrison Formation extinct ecosystem—a synthesis: Sedimentary Geology, v. 167, p. 309–355.

Turner-Peterson, C.E., 1986. Fluvial sedimentology of a major Uranium-bearing sandstone - A study of the Westwater Canyon Member of the Morrison Formation, San Juan Basin, New Mexico, *in* Turner-Peterson, C.E., Santos, E.S., and Fishman, N.S., eds, A Basin Analysis Case Study: The Morrison Formation, Grants Uranium Region, New Mexico: American Association of Petroleum Geologists, Studies in Geology 22, p. 47–76.

Ussami, N., Shiraiwa, S., and Dominguez, J., 1999, Basement reactivation in a sub-Andean foreland flexural bulge: The Pantanal wetland, SW Brazil: Tectonics, v. 18, p. 25–39.

Van de Graaff, F.R., 1972, Fluvial-deltaic facies of the Castlegate Sandstone (Cretaceous), East-Central Utah: Journal of Sedimentary Petrology, v. 42, p. 558–571.

Vorren, T.O., and Laberg, J.S., 1997, Trough Mouth Fans - Paeloclimate and ice-sheet monitors: Quaternary Science Reviews, v. 16, p. 865–881.

Weissmann, G.S., Hartley, A.J., Nichols, G.J., Scuderi, L.A., Olsen, M., Buehler, H, and Banteah, R., 2010, Fluvial form in modern continental sedimentary basins: Distributive fluvial systems: Geology, v. 38, p. 39–42.

Weissmann, G.S., Hartley, A.J., Scuderi, L.A., Nichols, G.J., Davidson, S.K., Owen, A, Atchley, S.C., Bhattacharyya, P., Chakraborty, T., Ghosh, P., Nordt, L.C., Michel, L., and Tabor, N.J., 2013, Prograding distributive fluvial systems - Geomorphic Models and Ancient Examples, *in* Dreise, S.G., Nordt, L.C., and McCarthy, P.L., eds, New Frontiers in Paleopedology and Terrestrial paleoclimatology: SEPM, Special Publication 104, p. 131–147.

**CAPTIONS**

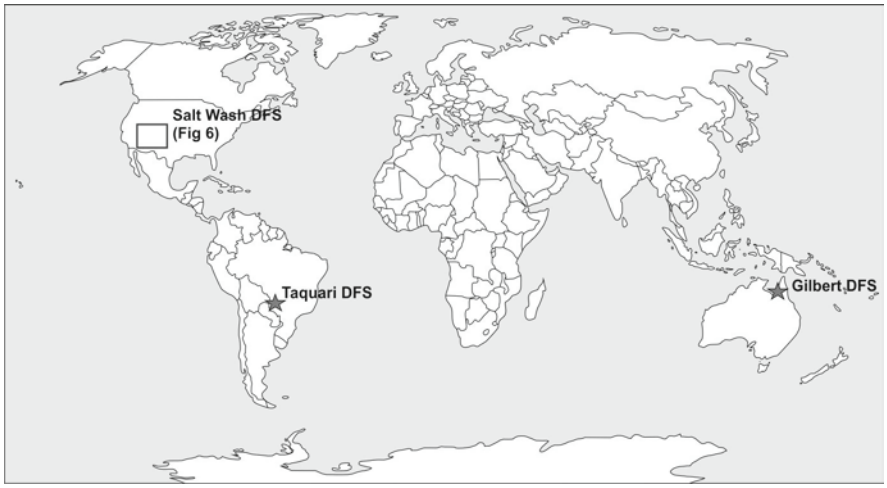


Figure 1 – Map showing the locations of DFSs studied. The stars represent modern datasets, and the box represents a dataset taken from the rock record.

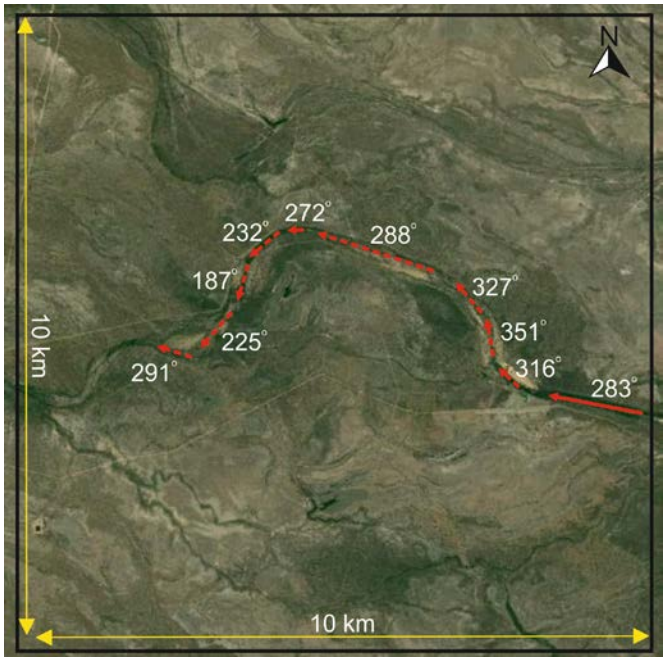


Figure 2 –The methodology in which paleocurrent readings were obtained from the Taquari and Gilbert DFSs. Up to ten channel orientations along a channel reach within a 10 km by 10 km cell were measured and centralized to a single point within the cell. This allows variability observed within vertical succession to be imitated.

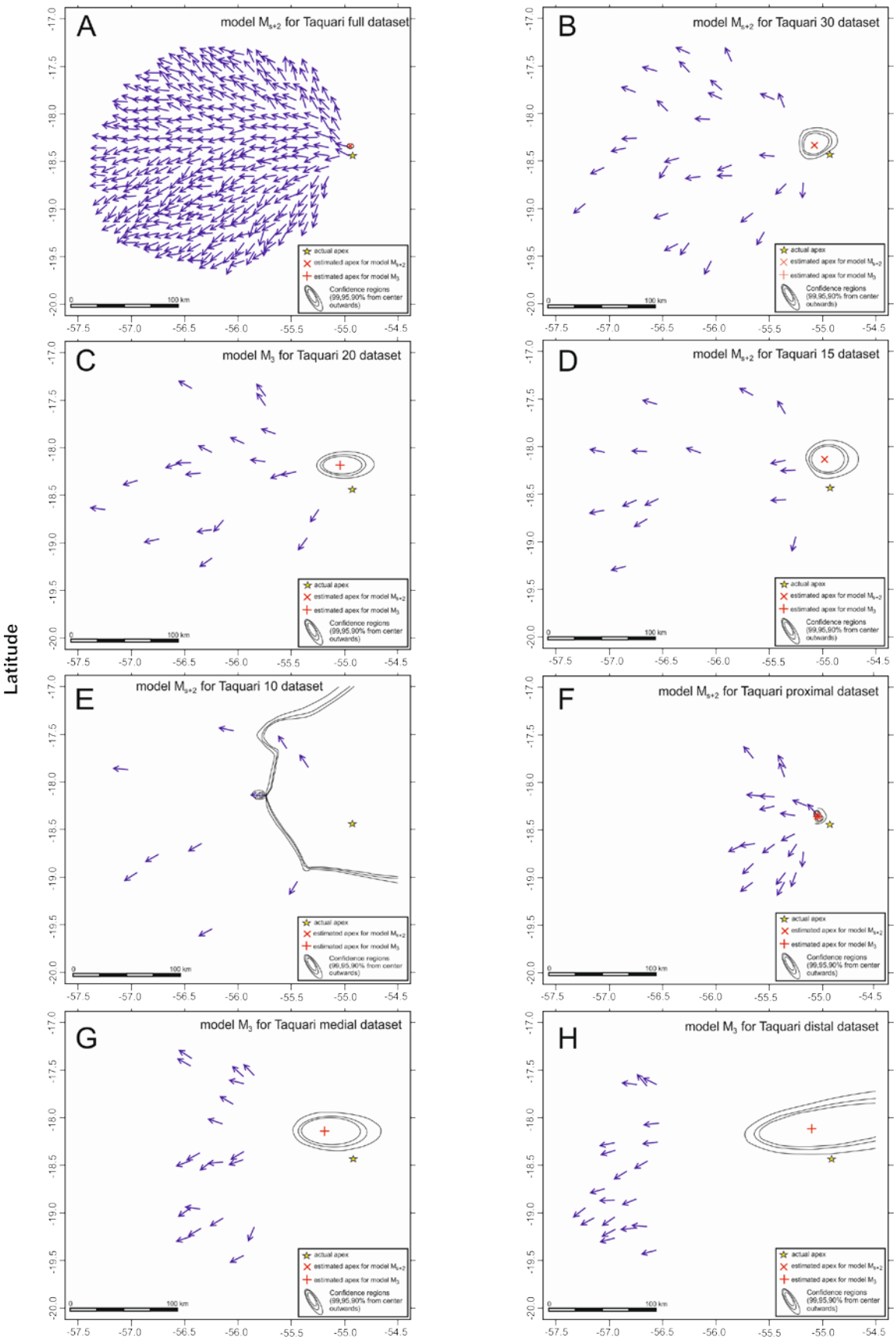
A
model $M_{s+2}$ for Taquari full dataset
B
model $M_{s+2}$ for Taquari 30 dataset
C
model $M_3$ for Taquari 20 dataset
D
model $M_{s+2}$ for Taquari 15 dataset
E
model $M_{s+2}$ for Taquari 10 dataset
F
model $M_{s+2}$ for Taquari proximal dataset
G
model $M_3$ for Taquari medial dataset
H
model $M_3$ for Taquari distal dataset
actual apex
estimated apex for model $M_{s+2}$
estimated apex for model $M_3$
Confidence regions (99,95,90% from center outwards)
100 km
Latitude
Longitude

Figure 3 –Results of analyses of various subsets of the Taquari DFS dataset. The full extent of the DFS can be seen in part A, as it shows the full dataset across the whole DFS. A) model $M_{s+2}$ using a full dataset; B) model $M_{s+2}$ using 30 locations; C) model $M_3$ using 20 locations; D) model $M_{s+2}$ using 15 locations; E) – model $M_{s+2}$ using 10 locations; F) model $M_{s+2}$ using only proximal locations; G) model $M_3$ using only medial locations; H) model $M_3$using only distal locations. Blue arrows represent mean directions at each site. All data used can be found in the data repository.

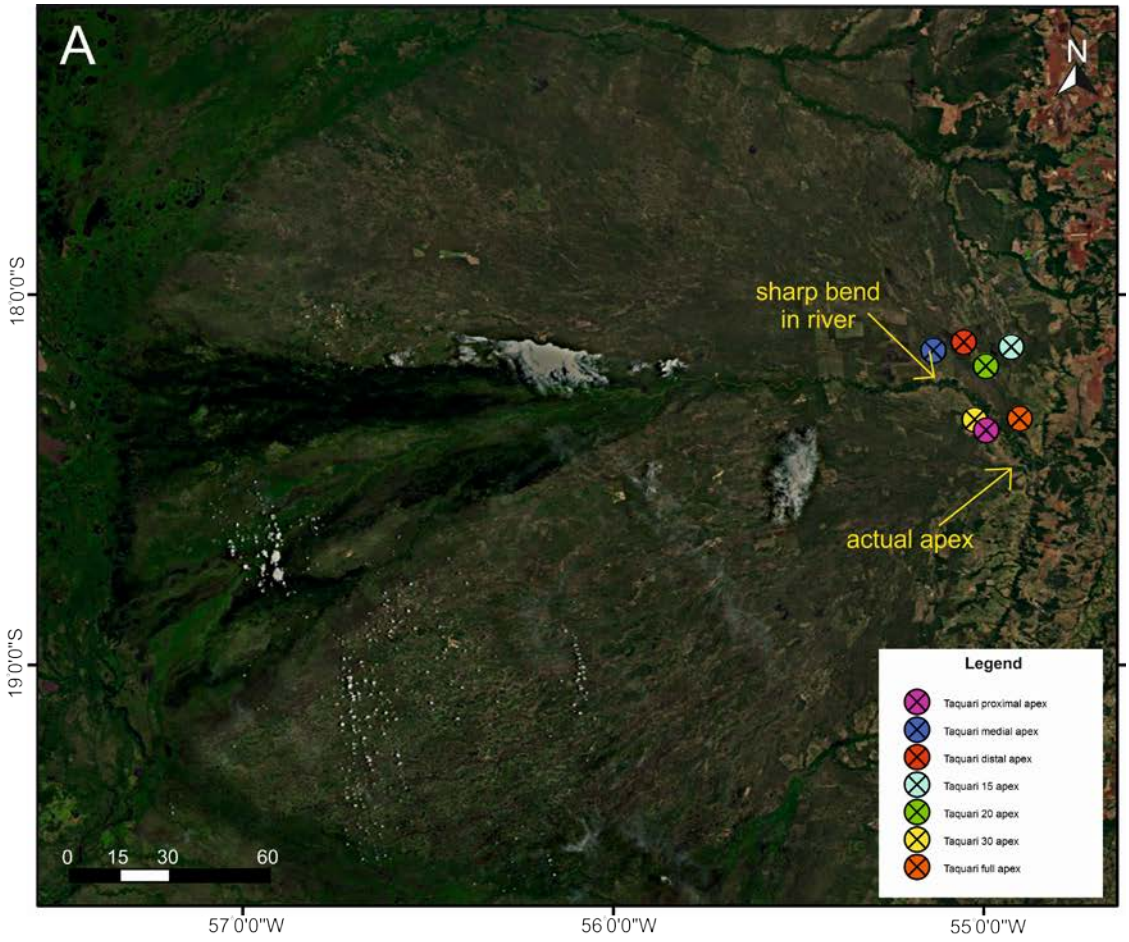
A
N
sharp bend
in river
actual apex
Legend
Taquari proximal apex
Taquari medial apex
Taquari distal apex
Taquari 15 apex
Taquari 20 apex
Taquari 30 apex
Taquari full apex
0 15 30 60
18°0'0"S
19°0'0"S
57°0'0"W
56°0'0"W
55°0'0"W

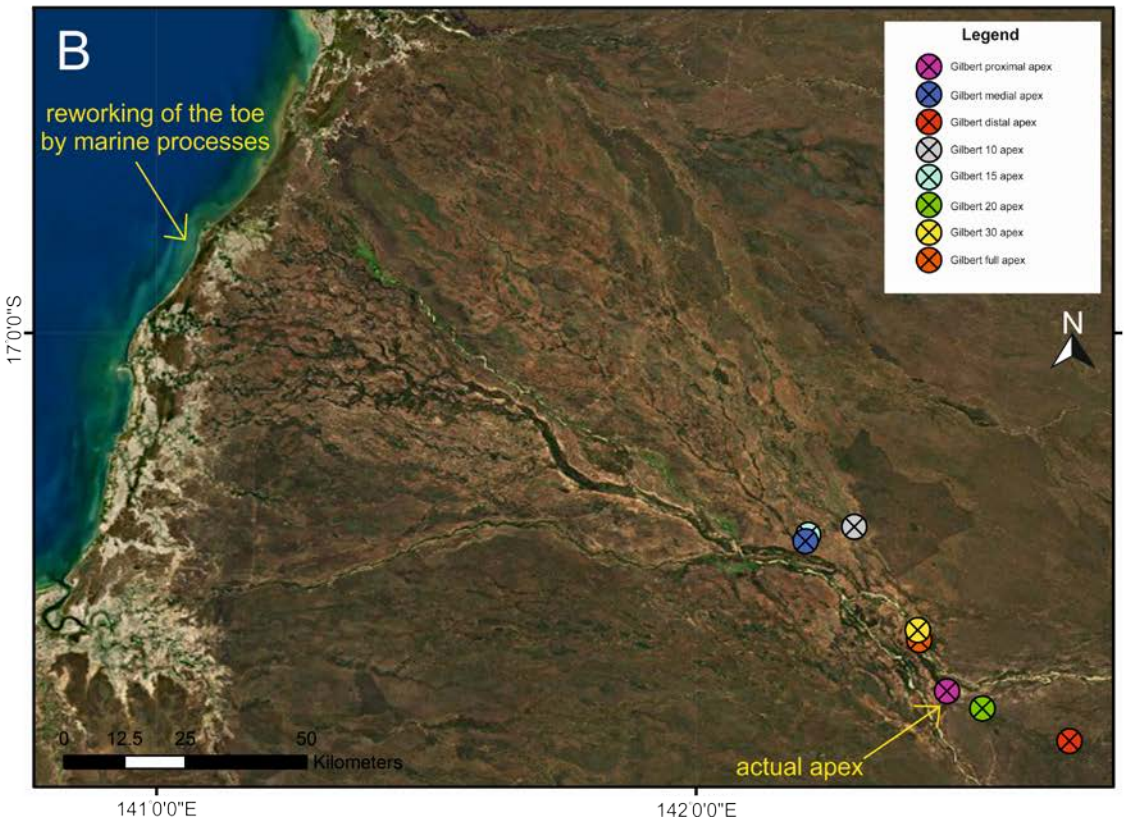
B
reworking of the toe
by marine processes
Legend
Gilbert proximal apex
Gilbert medial apex
Gilbert distal apex
Gilbert 10 apex
Gilbert 15 apex
Gilbert 20 apex
Gilbert 30 apex
Gilbert full apex
N
0 12.5 25 50
Kilometers
actual apex
17°0'0"S
141°0'0"E
142°0'0"E

Figure 4 – Results for analyses conducted on the A) Taquari DFS and B) Gilbert DFS. All data points used in each model can be seen in Figure 4 (Taquari DFS) and Figure 5 (Gilbert DFS).

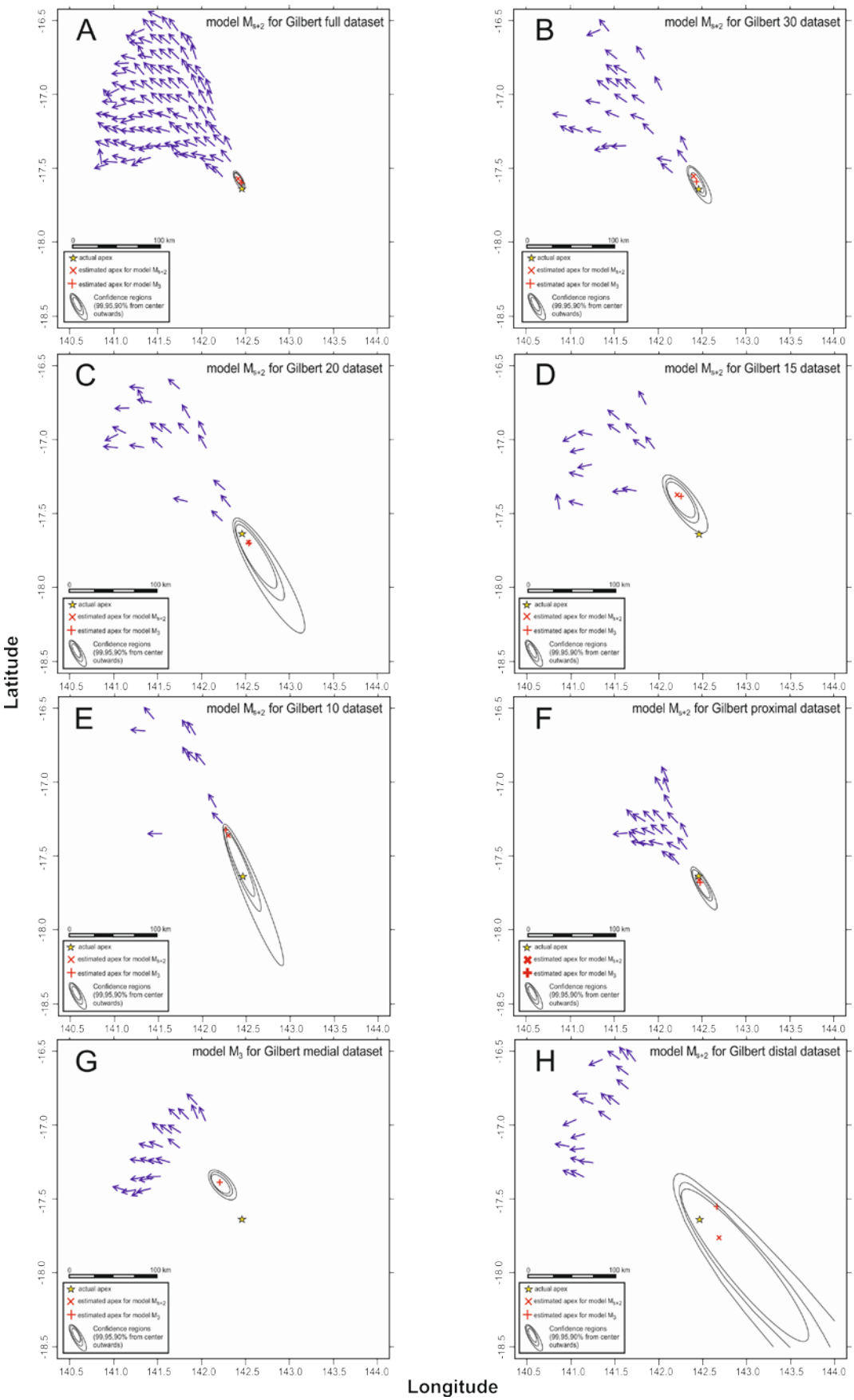
A
model $M_{s+2}$ for Gilbert full dataset
B
model $M_{s+2}$ for Gilbert 30 dataset
C
model $M_{s+2}$ for Gilbert 20 dataset
D
model $M_{s+2}$ for Gilbert 15 dataset
E
model $M_{s+2}$ for Gilbert 10 dataset
F
model $M_{s+2}$ for Gilbert proximal dataset
G
model $M_3$ for Gilbert medial dataset
H
model $M_{s+2}$ for Gilbert distal dataset
0
100 km
actual apex
estimated apex for model $M_{s+2}$
estimated apex for model $M_3$
Confidence regions (99,95,90% from center outwards)
-16.5
-17.0
-17.5
-18.0
-18.5
140.5
141.0
141.5
142.0
142.5
143.0
143.5
144.0
Latitude
Longitude

Figure 5 – Results of analyses of various subsets of the Gilbert DFS dataset. The full extent of the DFS can be seen in part A, as it shows the full dataset across the whole DFS. A) model $M_{s+2}$ using a full dataset; B) model $M_{s+2}$ using 30 locations; C) model $M_{s+2}$ using 20 locations; D) model $M_{s+2}$ using 15 locations; E) model $M_{s+2}$ using 10 locations; F) model $M_{s+2}$ using only proximal locations; G) model $M_3$ using only medial locations; H) model $M_{s+2}$using only distal locations. Blue arrows represent mean directions at each site. All data used are present in the data repository.

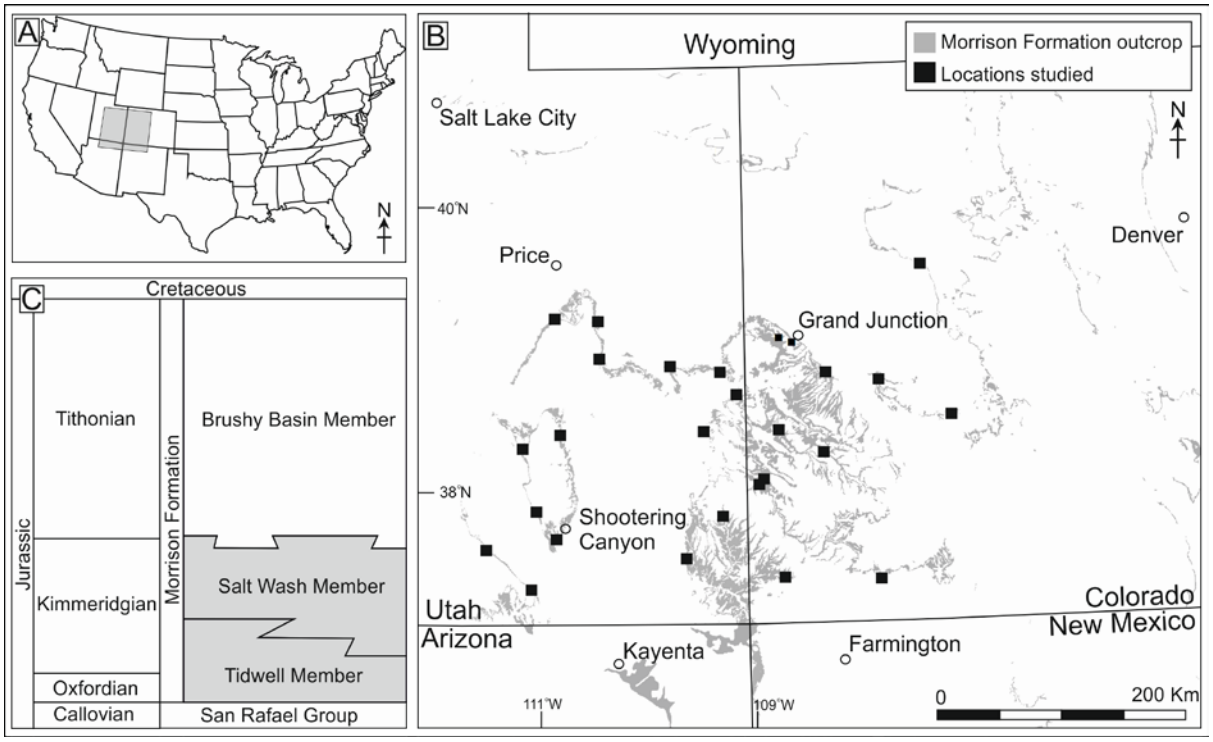


Figure 6 – A) Location of the study area. B) Location map of the study area showing the location of sites studied relative to Morrison Formation outcrop. C) Stratigraphy of the study area.

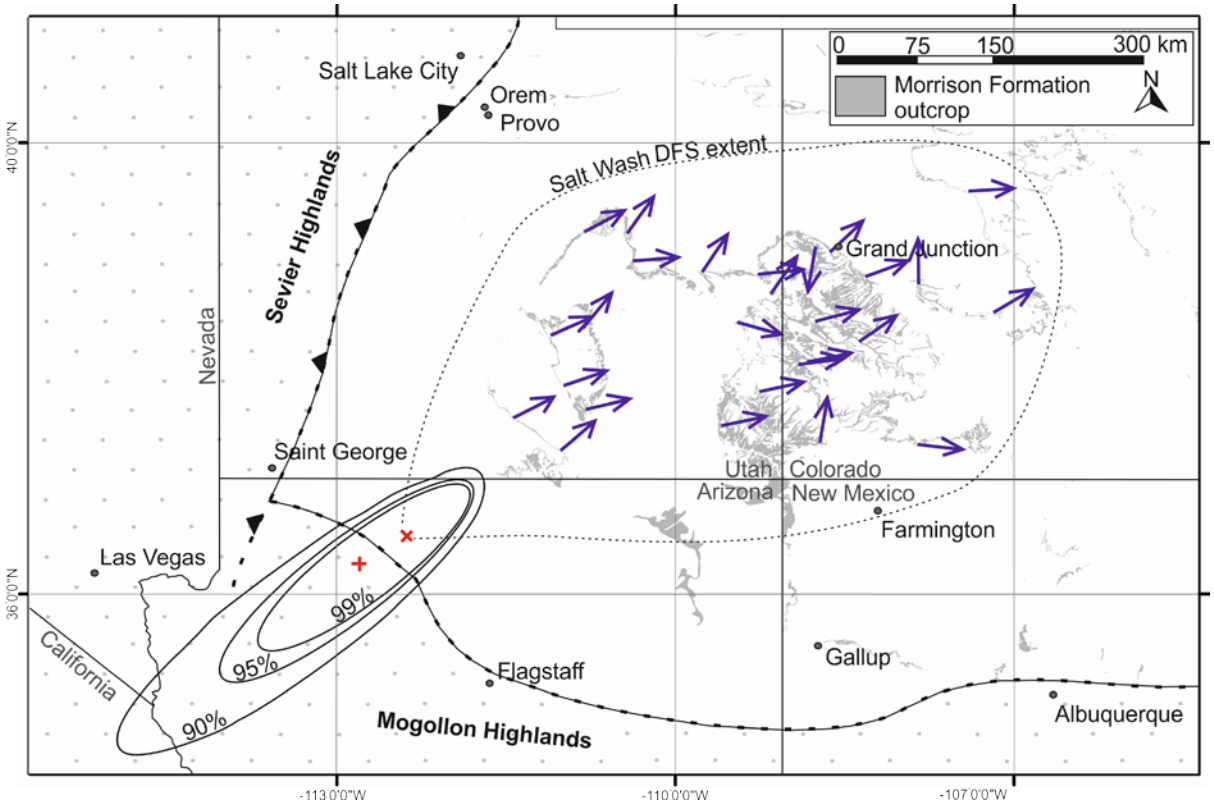


Figure 7- Location of the Salt Wash estimated apex. x indicates model $M_{s+2}$, + indicates model $M_3$. Sevier and Mogollon Highlands extent is based on Dickinson and Gehrels (2008), Spencer et al. (2011), and results obtained in this study.

| Model | Distribution of $\boldsymbol{\theta_{ij}}$ | Parameters | Description |
|---|---|---|---|
| $M_{2s}$ | $M(\mu_i, \kappa_i)$ | $\mu_1, \dots, \mu_s, \kappa_1, \dots, \kappa_s$ | Largest model. Used to assess how well model $M_{s+2}$ fits the data. Single apex is not assumed |
| $M_{s+2}$ | $M(\mu_i(\mathbf{c}), \kappa_i)$ | $\mathbf{c}, \kappa_1, \dots, \kappa_s$ | Single apex is assumed with possibly different concentrations |
| $M_3$ | $M(\mu_i(\mathbf{c}), \kappa)$ | $\boldsymbol{c}, \kappa$ | Simplest model in which a single apex is assumed with sites possessing equal concentrations |

Table 1: Summary description of the mathematical models used within the code.

| Dataset | Model | Estimated apex longitude | Estimated apex latitude | *p.fit* | *p.same* | Distance from actual apex (km) | % of total DFS length away from true apex |
|---|---|---|---|---|---|---|---|
| Taquari full | $\boldsymbol{M_{s+2}}$ | **-54.9586** | **-18.3241** | 0 | | 13.1 | 5.24 |
| | $M_3$ | -54.8865 | -18.3405 | | 0 | 12 | |
| Taquari 30 | $\boldsymbol{M_{s+2}}$ | **-55.0765** | **-18.3269** | 0 | | 19.7 | 7.9 |
| | $M_3$ | 182.5861 | 31.7826 | | 0 | | |
| Taquari | $M_{s+2}$ | -55.043 | -18.1852 | 0.026 | | 30.7 | |

| | | | | | | | |
|---|---|---|---|---|---|---|---|
| 20 | $\boldsymbol{M_3}$ | **-55.0473** | **-18.1841** | | 0.228 | 30.6 | 12.2 |
| Taquari 15 | $\boldsymbol{M_{s+2}}$ | **-54.9806** | **-18.1331** | 0.023 | | 34.2 | 13.7 |
| | $M_3$ | 1856.0042 | -428.3613 | | 0 | | |
| Taquari 10 | $M_{s+2}$ | 5378.9292 | 2865.7045 | 0 | | | |
| | $M_3$ | 4960.0871 | -1285.2779 | | 0 | | |
| Taquari proximal | $\boldsymbol{M_{s+2}}$ | **-55.0465** | **-18.3555** | 0.168 | | 15.4 | 6.2 |
| | $M_3$ | -55.0466 | -18.3555 | | 0.001 | 15.4 | |
| Taquari medial | $M_{s+2}$ | -55.2493 | -18.1247 | 0.002 | | 42.5 | |
| | $\boldsymbol{M_3}$ | **-55.1842** | **-18.1423** | | 0.194 | 42.4 | 17.0 |
| Taquari distal | $M_{s+2}$ | -54.9469 | -18.0375 | 0.001 | | 44.8 | |
| | $\boldsymbol{M_3}$ | **-55.1051** | **-18.12** | | 0.461 | 40.3 | 16.1 |

Table 2: Results from analyses of the Taquari DFS datasets. The actual apex is located at longitude: -54.930619, latitude -18.439154.

| Dataset | Model | Estimated apex longitude | Estimated apex latitude | *p.fit* | *p.same* | Distance from actual apex (km) | % of total DFS length away from true apex |
|---|---|---|---|---|---|---|---|
| Gilbert full | $\boldsymbol{M_{s+2}}$ | **142.4137** | **-17.5691** | 0 | | 9.4 | 5.5 |
| | $M_3$ | 142.4527 | -17.5952 | | 0 | 5 | |
| Gilbert 30 | $\boldsymbol{M_{s+2}}$ | **142.4109** | **-17.5507** | 0 | | 11.3 | 6.7 |
| | $M_3$ | 142.4433 | -17.5884 | | 0 | 10 | |
| Gilbert 20 | $\boldsymbol{M_{s+2}}$ | **142.531** | **-17.696** | 0 | | 9.5 | 5.6 |
| | $M_3$ | 142.5358 | -17.6998 | | 0.001 | 10.2 | |
| Gilbert 15 | $\boldsymbol{M_{s+2}}$ | **142.2081** | **-17.3743** | 0 | | 39.8 | 23.4 |
| | $M_3$ | 142.2498 | -17.3847 | | 0 | 36.3 | |
| Gilbert 10 | $\boldsymbol{M_{s+2}}$ | **142.2936** | **-17.3595** | 0.072 | | 35.8 | 21.1 |
| | $M_3$ | 142.2643 | -17.3205 | | 0.008 | 41 | |
| Gilbert proximal | $\boldsymbol{M_{s+2}}$ | **142.4653** | **-17.6638** | 0.038 | | 2.7 | 1.6 |
| | $M_3$ | 142.4824 | -17.6776 | | 0.075 | 4.7 | |
| Gilbert medial | $M_{s+2}$ | 142.1936 | -17.3747 | 0.035 | | 40.8 | |
| | $\boldsymbol{M_3}$ | **142.2031** | **-17.3861** | | 0.549 | 39.2 | 23.1 |
| Gilbert distal | $\boldsymbol{M_{s+2}}$ | **142.6921** | **-17.7562** | 0.001 | | 27.7 | 16.3 |
| | $M_3$ | 142.6625 | -17.5533 | | 0 | 23 | |

Table 3: Results from analyses of the Gilbert DFS datasets. The actual apex is located at longitude: 142.463608, latitude -17.638897.

| Dataset | Model | Eastings | Northings | *p.fit* | *p.same* |
|---|---|---|---|---|---|
| Salt Wash full | $\boldsymbol{M_{s+2}}$ | **-112.3772** | **36.4943** | 0 | |
| | $M_3$ | -112.7842 | 36.2438 | | 0 |

Table 4: Results from analyses of the Salt Wash dataset.